

Spatial Position–Force Perception for a Soft Parallel Joint via Pressure-Deformation Self-Sensing

Yinyin Su , Xiaojiao Chen , Zhonggui Fang , Dong Liu , James Lam , *Fellow, IEEE*,
and Zheng Wang , *Senior Member, IEEE*

Abstract—Robotic perception, the ability to detect internal position and orientation and external stimuli, enables robots to interact safely with humans and manipulate safely in unstructured environments. Soft robots hold an inherited leading edge over rigid-body robots in terms of interaction compliance and safety, but they still require dedicated sensors when accuracy or force interaction is concerned. However, perceiving high-dimensional multimodal information for the soft robot is still a challenge. Previous works focused more on single-type perception for one-degree-of-freedom (DoF) soft robots with complicated sensor fabrications. In this work, inspired by the human muscle perceptive system, we proposed a similar synthetic sensing module with embedded pressure and laser range sensors. Then, a three-DoF [one-DoF axial motion (± 25 mm) and two-DoF omnidirectional bending motion ($\leq 30^\circ$)] soft parallel robot based on the self-sensing origami actuator is developed. The actuator- and joint-level perceptive models are derived with embedded sensors to realize 3-D position and force perception simultaneously. It is

validated by the dedicated position and orientation, and axial force and bending torque perception experiments (phase lag ≈ 450 ms) in an origami soft parallel joint (OSPJ) with four actuators. The method may pave the way for an inexpensive internal sensing method, not affecting the soft actuator's performance, and provides possibilities for the soft robots to achieve multimodal estimation for closed-loop control and interaction with the physical environment.

Index Terms—3-D position and force perception, internal sensing method, origami soft parallel joint (OSPJ), robotic perception.

NOMENCLATURE

l_{mi}	Actuator's measured length.
l_0, l_c	Initial axial length and edge length.
l_{\max}, l_{\min}	Maximum and minimum axial length.
α	Actuator's bending angle.
d_a	Actuator's equivalent diameter.
F_a	Actuator's output force.
P	Internal relative pressure.
T_a	Actuator's bending torque.
F_e	Actuator's external exerted force.
M_e	Actuator's external exerted torque.
F_c	Distributed force.
i	i th actuator for the joint.
n	Number of actuators.
l_i	i th actuator's arc length.
d_s	Joint plane's diameter.
L, κ, ϕ	Backbone's arc length, curvature, and rotation angle.
r	Backbone curvature radius.
β	Backbone bending angle.
$\mathcal{V}_{js}, \mathcal{V}_{32}$	Spatial twist in frame $\{s\}$ and $\{2\}$.
\mathbf{T}	Transformation matrix for the joint.
\mathbf{R}, \mathbf{p}	Robotic rotation matrix and position.
F_{es1}, F_{es2}, \dots	Robotic external stimuli.
\mathbf{F}, \mathbf{T}	Generated force and torque vector of the joint.
F_z, T_x, T_y	External force and torques.

I. INTRODUCTION

ROBOTIC perception, including self-state estimation, contact and collision modeling, and external environmental

Zhonggui Fang, Dong Liu, and Zheng Wang are with the Department of Mechanical and Energy Engineering, Southern University of Science and Technology, Shenzhen 518055, China (e-mail: 11930523@mail.sustech.edu.cn; deniss.liudong@gmail.com; wangz@sustech.edu.cn).

This article has supplementary material provided by the authors and color versions of one or more figures available at <https://doi.org/10.1109/TMECH.2023.3340342>.

Digital Object Identifier 10.1109/TMECH.2023.3340342

mapping, is one of the fundamental necessities for closed-loop control in intelligent robots [1]. It can improve safety and task performance during robot operations in an unstructured environment [2], [3], [4]. As for the conventional rigid robots, perceptions are feasible to realize the state and contact observability with the availability of accurate models [2]. However, the high nonlinearity and inherent compliance limit implementations in the soft counterparts [5], [6]. Diverse approaches have been explored to endow soft robots with perception, categorized into internal and external sensing methods.

The external sensing method depends on the externally installed sensors, like the force sensor or visual camera. Recently, various existing solutions have been reported, such as depth vision [7] to control the stiffness of a tendon-driven robot, the honeycomb pneumatic network arm [8] with the motion capture system, and soft surgery robots with intrinsic force sensors to perceive stimuli [9]. Due to the large size of those sensors, applying them in compact sensing situations is challenging [10].

Conversely, the internal sensing method is realized by the embedded sensors in the robots' body and is not restricted by coordinate transformation problems from the external sensors. It has direct and indirect implementations. The former uses sensory information directly, while the latter builds models to estimate states. Pioneering direct works such as curvature sensors for bending actuators [11] and infrared sensors for bellows actuator [10] have been presented. More indirect solutions use the robot model to estimate force [12], [13], [14] or position [15], [16], [17] from other information sources, utilizing the compact sensors to perceive more complicated information. However, these works overlook the multimodal perception, the ability to perceive multiple physical parameters, which is one of the biggest challenges in perception for soft robots [1], [18].

In this article, inspired by the muscle spindles and Golgi tendon organ (GTO) receptors in the human muscle perceptive system, we propose a pressure-deformation dual-modal self-sensing actuator (PDDSA). By incorporating pressure and laser sensor chips into the designed printed circuit board (PCB), the PDDSA can measure the real-time states with no complicated fabrication and no compromise in compliance. Based on the PDDSA, a three-degree-of-freedom (DoF) origami soft parallel joint (OSPJ) is designed, enabling the soft robot to achieve high-dimensional position and force perceptions simultaneously, which is still a challenge in the soft robotic field [19]. To this end, the analytical actuator-level force model, the joint-level position, and the force model are developed to realize 3-D position and three-axial force estimations. The path trajectory and force experiments are designed to validate the PDDSA and the proposed high-dimensional models. This sensing module can be easily applied to elastic pneumatic actuators and composed as a sensing network with the same prototype. Also, the results demonstrated in our works can provide real-time position and force feedback to control soft robots.

The primary contributions of this work are as follows.

- 1) Concept and design of a PDDSA with origami are presented inspired by the human muscle perceptive system.
- 2) An analytical force model for the PDDSA is derived considering the bending angle's effect.

- 3) Based on the actuator force model (AFM) and the sensing method, the spatial perceptive model is derived for the three-DoF soft parallel robot, with the ability to perceive 3-D position and three-axial forces simultaneously.
- 4) An OSPJ and the dedicated control system are designed to demonstrate the effectiveness and accuracy of the spatial perceptive scheme, with real-time position perceptions in various path-tracking experiments and force estimations in different initial states.

The rest of this article is organized as follows. We first quickly overview the related work in Section II. The concept and design of the PDDSA and the soft robot are presented in Section III. The AFM, the joint-level position, and the force perceptive model are proposed in Section IV. Section V describes the control scheme for the soft robot. The robotic system is then realized and verified by the experimental results in Section VI. Finally, Section VII concludes this article.

II. RELATED WORK

Most recently, soft robots with abilities to realize both internal states (e.g., positions and orientations) and external stimuli (e.g., interactive forces) simultaneously, the most representative multimodal observation applications, have been reported. A fiber-reinforced soft prosthetic hand integrated with curved, elongation, and force sensors, all fabricated by photonic strain sensors, is reported to recognize the objects [20]; a soft gripper with proprioceptive and haptic sensing ability via soft somatosensitive actuators is reported in [21], and data-driven approaches via embedded strain sensors [1] and flex sensors [18] for the soft gripper are also explored to realize position and force estimations. Although the realized prototypes demonstrate the potential, they focus more on simple robotic systems, such as one-DoF or planar robots, due to current sensor configurations [18].

As for soft pneumatic robots [22], approaches to realizing multimodal observation with soft sensors based on the actuator's elastic chamber and embedded off-the-shelf pressure sensors have been explored recently. A tendon-driven soft monolithic robotic finger realizes bending position and mechanical pressure sensing by different deformed sensing chambers and pressure sensors [13], [23]. A similar sealed sensing body is also introduced in [24] for a soft gripper to measure the contact force and the bending actuator's curvature. In our previous works [2], [25], soft grippers with dedicated antagonistic pair of pneumatic actuators via pressure sensors are designed to measure real-time one-DoF displacement and grasping force. The relationships between pressure and measured variables in the abovementioned works are all built based on the sealed deformed chamber and the same number of moles of the gas and are calibrated experimentally. According to Boyle's law, the calibrated results may be easily affected by gas temperature in the sealed chamber, where the deformed chamber does work on the internal sealed gas. Moreover, these sealed sensing modules embedded in the soft robots passively sometimes generate antiderived forces, reducing the soft robots' performance.

Estimating the real-time system states for soft robots by utilizing the raw data from the embedded sensors is another

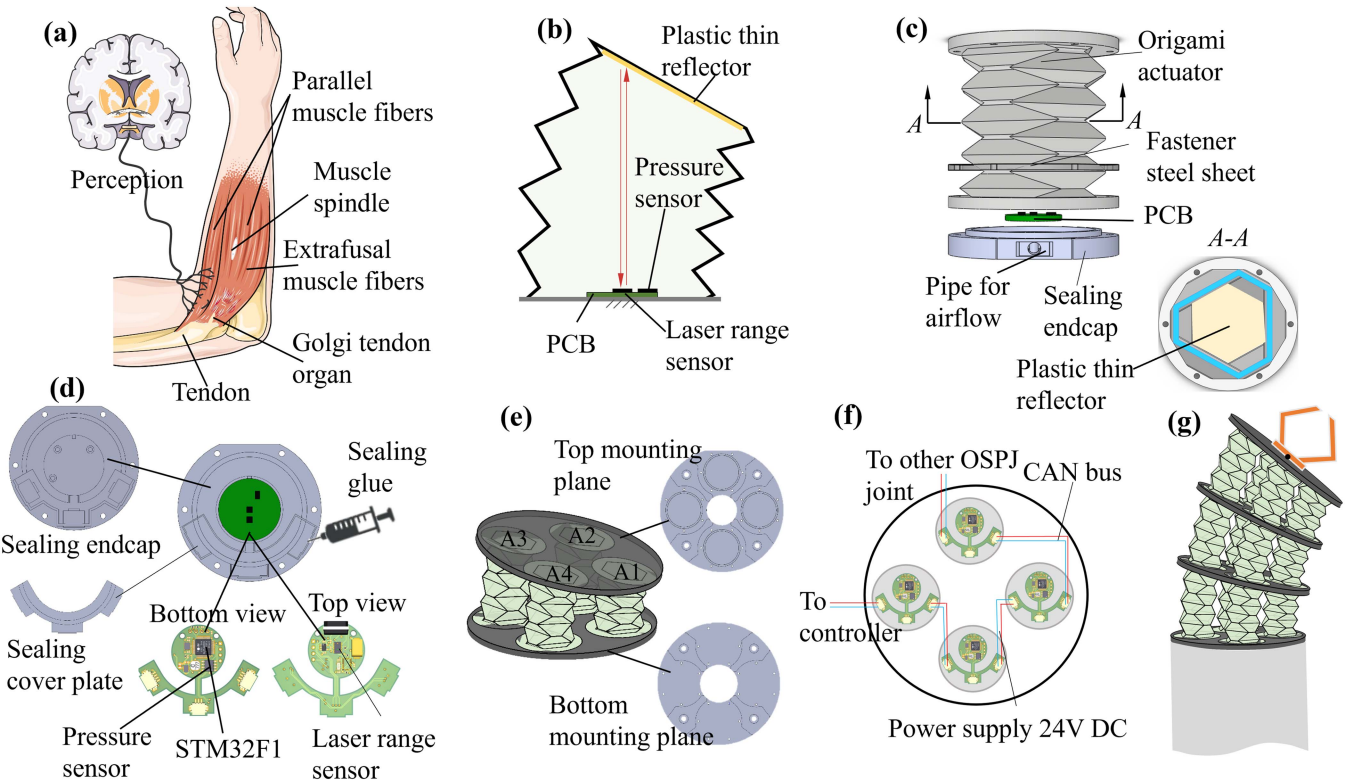


Fig. 1. (a) Perceptive system of human muscle. (b) Concept of the proposed PDDSA inspired by human muscle. (c) Design of the PDDSA. (d) Design and assembly of the sensing module. (e) OSPJ with four origami actuators. (f) Sensor network for the OSPJ. (g) Soft manipulator with three stacked OSPJs.

challenge [19]. Model-free and model-based approaches have been investigated. Model-free strategies are almost data driven connected with machine learning schemes, for example, force and position perception via embedded soft sensors and recurrent neural networks (RNNs) [1], [19] or RNN-based adaptive unscented Kalman filter (RNN-AUKF) [18], learning kinematic by both feedforward neuronal network and long short-term memory (LSTM) [26], realizing precise control for soft robots by the Koopman-based approach [27], [28], and estimating the posture of a soft arm via the k -nearest neighbors regression [29]. Although these data-driven approaches improve the estimation accuracy, they require large sets of data and expensive computational power, and case-by-case pretraining models have somewhat limited their applications [5]. Model-based approaches that depend mostly on steady-state assumptions, such as constant curvature [30], variable curvature [31], and Cosserat rod [32], could be realized without extra computational sources and extended to soft robots with similar configurations [5].

III. CONCEPT AND DESIGN

The presented perceptive soft robot is inspired by the human muscle's perceptive system, as shown in Fig. 1(a), where human proprioceptive receptors are composed of two essential organs: muscle spindles and GTO. The extrafusal muscle fiber acts as a motor unit to generate force and movement. With different contractions or elongation of parallel muscle fibers, the human joint outputs high-dimensional movements. The muscle spindles

TABLE I
GEOMETRY PARAMETERS OF THE ORIGAMI ACTUATOR

Initial height (l_0)	50.00 mm
Diameter of circumcircle of end (d_a)	41.00 mm
Initial height of one element (h_0)	5.5 mm
Initial dihedral angle of two trapezoid facets (θ_0)	80°
Length of short side of trapezoid (a)	9.35 mm
Length of long side of trapezoid (b)	31.27 mm
Thickness of actuator	1.3 mm

are located inside and parallel to the extrafusal muscle fibers, detecting changes in the length of the muscle, while the GTO lies at the interface between a muscle and its tendon, sensing changes in muscle tension [33]. The two pieces of information are both processed by the brain to realize perceptions. By imitating the human muscle receptors, a self-sensing pneumatic actuator is designed to implement perception with embedded pressure and laser range sensors to measure internal tension and length, as illustrated in Fig. 1(b).

A pneumatic elastic actuator with an origami structure is employed to construct the PDDSA, as shown in Fig. 1(c). As mentioned in [10], [34], and [35], the presented origami actuator has various advantages, such as scalability, reduced assembly, and larger radial stiffness than the axial stiffness, guiding the actuator's motion along the axial direction and generating larger force. It has a pneumatic chamber and a pattern sheet, as shown in Fig. 1(a). The detailed geometry parameters of the actuator are listed in Table I. Both the actuator body and the top cover are manufactured by molding with polypropylene rubber, and

the bottom is sealed by the sealing endcap, 3-D printed by Polyamide. A plastic thin reflector is glued on the internal top cover, as shown in Fig. 1(b). It provides a smoother reflector for the laser sensor and ensures that the reflector surface is flat, as the internal pressure leads to an arc-shaped top cover, decreasing the accuracy of an actuator's measured range. We design a PCB where pressure and laser range sensor chips are incorporated, as shown in Fig. 1(d). The sensor board is located at the center of the sealing endcap and covered by a sealing cover plate. All the sealing supporters are glued by the sealing epoxy glue. The two general interfaces, including controller area network (CAN) and supply power, are designed to connect with other sensor boards or microcontrollers. In addition, the PCB also establishes other redundant install points for other types of sensors, such as inertial measurement unit (IMU) sensors and temperature sensors, to extend the function.

To realize high-dimensional position and force perceptions, a soft parallel joint, like the human joint, is designed based on the PDDSA, as shown in Fig. 1(e). It consists of two parts: two hard circle planes (black area) 3-D printed by polylactic acid (PLA) to install soft actuators and individual soft pneumatic actuators (green area) installed along the hard plane's periphery. It has three DoFs: one DoF for axial motion and two DoFs for omnidirectional bending motions. The equal deformations of all individual soft actuators lead to axial movements, while the different deformations of the actuators lead to different bending angles and bending directions. A series of soft parallel joints can be stacked easily as a soft manipulator, as shown in Fig. 1(g). In this work, we focus on the characteristics of the soft parallel joint. By the convenient interface of the sensor board, all individual actuators are connected as a sensory network for the OSPJ, as shown in Fig. 1(f). All sensory information is collected and encoded by the microcontroller STM32F1 in each actuator, broadcasted on the CAN bus, and powered by 24-V dc.

IV. MODELING FOR POSITION AND FORCE PERCEPTION

In this section, we first describe high-dimensional position and force perceptive strategy. Then, analytical actuator- and joint-level position and force observers are derived.

A. Proposed Perceptive Strategy

As shown in Fig. 1(a), the human perceives high-dimensional position and force by processing the information in the brain from the receptors in muscles. Similarly, the spatial perception scheme is proposed for a large collection of OSPJs driven by cylinder-like elastomeric actuators. The approach to the OSPJ is summarized in Fig. 2. It is divided into three steps to decode the internal and external behaviors: 1) the joint position model (JPM) perceives the kinematic states through the embedded laser range sensors; 2) the proposed AFM computes the actuator's generated force by incorporating each actuator's internal pressure and configuration information from the JPM; and 3) the joint force model (JFM) accumulates the forces from actuators and perceive the external forces for the OSPJ.

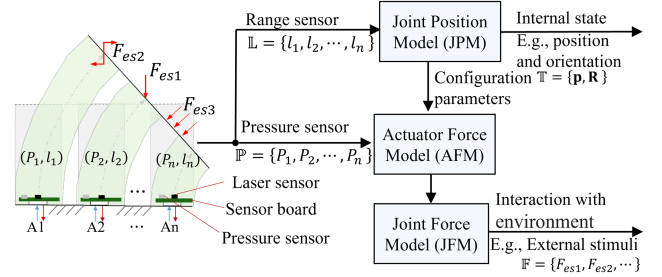


Fig. 2. Spatial perception scheme for the soft parallel robotic joint. The green and gray cylinders are the soft actuator's after and before deformation, respectively. P_i and l_i (i is the i th actuator, $i = 1, \dots, n$) are the sensory information for the A_i actuator, with red and blue arrows denoting negative and positive pressure, respectively. F_{es1} , F_{es2} , and F_{es3} are the external stimuli.

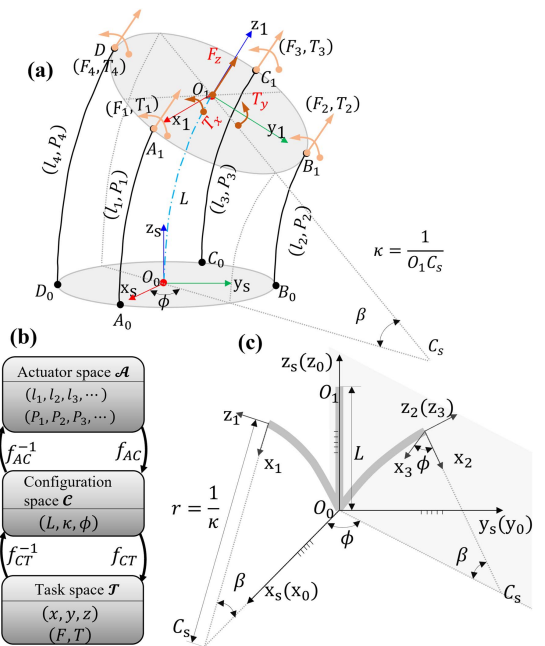


Fig. 3. Modeling for the OSPJ. (a) Schematic of the joint ($n = 4$) and its detailed geometric illustration. (b) Kinematic modeling. (c) Configuration space for the joint, varying from the initial position to the final position.

B. Joint Position Modeling

The JPM is derived for the OSPJ based on the constant curvature assumption [30]. It decomposes modeling into two procedures: 1) mapping from the actuator space \mathcal{A} to the configuration space \mathcal{C} and 2) mapping from the configuration space \mathcal{C} to the task space \mathcal{T} , as shown in Fig. 3(b). The actuator space describes the direct measured length and internal pressure in actuators; the configuration space represents arc parameters of the joint's backbone [the blue dash-dotted line in Fig. 3(a)]; and the task space denotes the end-effector's position and orientation, also interactive forces. f_{AC} and f_{CT} denote the forward kinematic from actuator space to task space, while f_{AC}^{-1} and f_{CT}^{-1} functions describe the inverse kinematic. l_i in \mathcal{A} represents the actuator's arc length and is computed by direct measured linear distance l_{mi} and bending angle β , $l_i = \frac{\beta l_{mi}}{\tan \beta}$. L , κ , and ϕ in \mathcal{C} describe the robot's geometrical configuration. We build these kinematic

models based on two assumptions: 1) constant curvatures for the joint and 2) all actuators within the joint are parallel. First, we model the function f_{AC} . As shown in Fig. 3(a), the relation between \mathcal{A} and \mathcal{C} is

$$L = l_i - \frac{d_s \beta}{2} \sin \left(\frac{2\pi(i-1)}{n} + \frac{\pi}{2} - \phi \right) \quad (1)$$

where d_s is the diameter of the joint's plane and β is the joint's bending angle. From (1), the three configuration parameters can be solved if and only if $n \geq 3$. Based on the geometries in Fig. 3(a), $n = 4$, the variables L , κ , and ϕ in \mathcal{C} are

$$\begin{aligned} L &= \frac{l_1 + l_2 + l_3 + l_4}{4}, \phi = \arctan \left(\frac{l_4 - l_2}{l_3 - l_1} \right) \\ \kappa &= \frac{2\sqrt{(l_4 - l_2)^2 + (l_3 - l_1)^2}}{(l_1 + l_3)d_s} \end{aligned} \quad (2)$$

with the length constraint

$$l_1 + l_3 = l_2 + l_4. \quad (3)$$

Second, we model f_{CT} through the product for exponentials (PoE) method. We extract the backbone of the joint to derive the homogeneous transformation matrix $\mathbf{T} \in SE(3)$, relating the endpoint coordinate frame to the starting point coordinate frame, as shown in Fig. 3(c). We define two spatial twists $\mathcal{V}_{1s} = [\omega_{1s} \ v_{1s}]^T \in \mathbb{R}^6$ to denote the in-plane transformation from frame {0} to frame {1} by bending angle β and $\mathcal{V}_{2s} = [\omega_{2s} \ v_{2s}]^T \in \mathbb{R}^6$ to denote the rotation transformation from frame {1} to frame {2} by rotation angle ϕ . ω_{js} and v_{js} ($j = 1, 2$) are the j th unit angular velocity and j th instantaneous velocity in the intermediate frames at the stationary frame {s} origin, respectively. v_{js} can be computed via $v_{js} = \dot{p}_{js} - \omega_{js} \times p_{js}$ when angular velocity is not equal to 0. p_{js} is the j th frame origin position vector expressed in {s}. The two angular velocities can be set as $\omega_{1s} = (0, 1, 0)$ and $\omega_{2s} = (0, 0, 1)$. Based on the geometry relations in Fig. 3(c), v_{1s} and v_{2s} can be expressed as $v_{1s} = (0, 0, r)$ and $v_{2s} = (0, 0, 0)$ respectively. Overall, the two spatial twists are

$$\begin{aligned} \mathcal{V}_{1s} &= [0 \ 1 \ 0 \ 0 \ 0 \ r]^T \\ \mathcal{V}_{2s} &= [0 \ 0 \ 1 \ 0 \ 0 \ 0]^T. \end{aligned} \quad (4)$$

At last, we rotate the frame {2} by $-\phi$ regarding to the z_2 -axis to present the final coordinate frame conveniently. Therefore, we define the twist

$$\mathcal{V}_{32} = [0 \ 0 \ 1 \ 0 \ 0 \ 0]^T \quad (5)$$

which is expressed in the frame {2}. So, the overall transformation matrix can be derived by applying the PoE formula

$$\mathbf{T} = e^{[\mathcal{V}_{2s}]\phi} e^{[\mathcal{V}_{1s}]\beta} e^{-[\mathcal{V}_{32}]\phi} \quad (6)$$

where the specific type of $e^{[\mathcal{V}_{2s}]\phi}$ is computed in Lie group theory. Expanding (6), the whole homogeneous transformation matrix \mathbf{T} for the joint, JPM, is

$$\mathbf{T} = \begin{bmatrix} \mathbf{R} & \mathbf{p} \\ \mathbf{0} & 1 \end{bmatrix}$$

$$\mathbf{R} =$$

$$\begin{bmatrix} \cos^2 \phi \psi + 1 & \sin \phi \cos \phi \psi & \cos \phi \sin \kappa L \\ \sin \phi \cos \phi \psi & \cos \kappa L - \cos^2 \phi \psi & \sin \phi \sin \kappa L \\ -\cos \phi \sin \kappa L & -\sin \phi \sin \kappa L & \cos \kappa L \end{bmatrix}$$

$$\mathbf{p} = [-\cos \phi \psi / \kappa \ \ -\sin \phi \psi / \kappa \ \ \sin \kappa L / \kappa]^T \quad (7)$$

$$\text{where } \psi = \cos \kappa L - 1.$$

In practice, the measured lengths from the range sensor cannot meet the constraint in (3) strictly due to the measured noises and compliance of the soft robot. Hence, we choose three adjacent actuators along the installed circle plane continually and average the obtained configuration parameters from (2). The four combined actuators are [1, 2, 3], [2, 3, 4], [3, 4, 1], and [4, 1, 2].

C. Force Modeling for the PDDSA

Before the JFM, the AFM, including generated axial force and bending torque, is explored to capture the relationship between forces and the actuator's internal pressure and arc length by considering the actuator's geometry and bending angle. The actual actuator's geometry parameters are listed in Table I; the bending angle is obtained from the above JPM, and the other variables in this model could be measured by the installed sensors or calibrated in actuator experiments. The AFM is derived based on the following assumptions: 1) the self-mass of the actuator is negligible; 2) the actuator has a constant curvature; 3) the actuator's radial expansion is negligible due to the origami shell pattern; 4) the air pressure changes slowly, and the actuator's deformation process is quasi-static; 5) the elastic stiffness along the wall of the actuator in each bending situation is equal and only related to actuator's axial length; and 6) the actuator's volume is unchanged if the arc length of the actuator is equal.

The actuator motion can be divided into two stages: 1) the internal pressure drives the actuator to move in the axial direction and 2) and the rigid support plane in the soft joint restricts the actuator to a bending situation due to the different deformed lengths of the actuators. According to the principle of virtual work, the work done by external forces equals the work done by internal forces [14]

$$\delta W_P + \delta W_S = \delta W_{F_e} + \delta W_{M_e} \quad (8)$$

where δW_P is the pressure-related work, δW_S is the stored energy of the actuator, and δW_{F_e} and δW_{M_e} are the works done by the external force and torque, respectively.

1) *Modeling for Axial Force F_a* : As shown in Fig. 4(a), the axial generated force F_a equals the external axial force F_e due to the force balance. In the actuator's first stage with no external torque where the actuator bending angle $\alpha = 0$, the work done by the external torque $\delta W_{M_e} = 0$. Therefore, according to (8), F_a comes from pressure-related force F_P and deformation-related forces F_S

$$F_a = F_P + F_S. \quad (9)$$

The force F_S only depends on the actuator's self-elastic deformation along the axial direction and can be represented

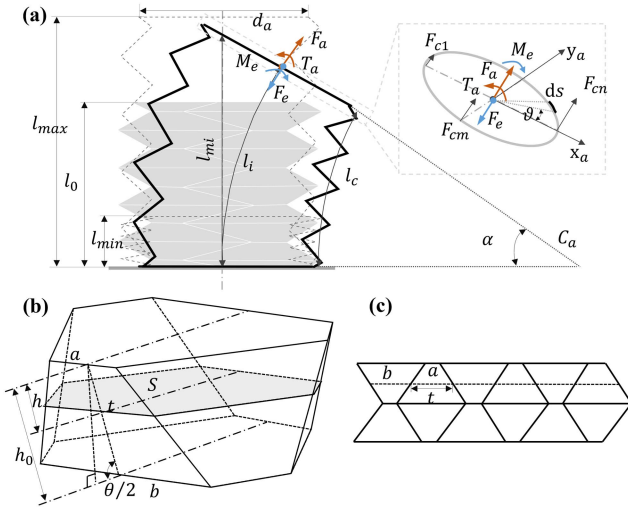


Fig. 4. Modeling for the origami actuator. (a) Schematic of the actuator and its bending situation. (b) Schematic of a single unit for an origami actuator. (c) Two-dimensional expanded pattern of the origami actuator.

as

$$F_S = -k\Delta l_i \quad (10)$$

where \$k\$ is the actuator's stiffness coefficient, and \$\Delta l_i\$ is the actuator's relative length, computed by \$l_i - l_0\$.

According to (8), the pressure generated force \$F_P\$ can be derived as

$$F_P = \frac{\delta W_P}{\delta l_i} = P \frac{\delta V_a}{\delta l_i} \quad (11)$$

where \$P\$ is the actuator's internal relative pressure and \$V_a\$ is the actuator's volume. We select the single origami unit from the presented actuator to compute the actuator's internal volume, as shown in Fig. 4(b). Moreover, we expand two origami units to the 2-D plane, as shown in Fig. 4(c), where the actuator's cross section has a constant circumference \$3(a+b)\$. \$a\$ and \$b\$ are the designed minimum and maximum lengths of the cross section, respectively. For the length of cross section \$t\$ at a given vertical distance \$h\$ from the short edge, \$t\$ can be computed by geometrical relationship, \$t = a + \frac{b-a}{h_0}h\$. Hence, the cross-sectional area \$S\$ is

$$S = \frac{\sqrt{3}}{4} \left(-\frac{2(b-a)^2}{h_0^2}h^2 + \frac{2a^2 - 4ab + 2b^2}{h_0}h + a^2 + 4ab + b^2 \right). \quad (12)$$

The internal volume of a unit can be computed by

$$V = \int_0^{h_0} S dh = \frac{\sqrt{3}(2a^2 + 5ab + 2b^2)}{6} h_0. \quad (13)$$

The actuator's volume \$V_a\$ can be derived from the sum volume of the number of origami units \$n_s\$

$$V_a = \frac{\sqrt{3}(2a^2 + 5ab + 2b^2)}{6} n_s h_0 \quad (14)$$

where \$l_i = n_s h_0\$. Substituting (14) into (11), the pressure-related generated force can be derived as

$$F_p = \frac{\sqrt{3}(2a^2 + 5ab + 2b^2)}{6} P. \quad (15)$$

The larger axial force generated by pressure can be obtained for the smaller bending angle for the pneumatic actuator, as mentioned in the previous bending experiments [34]. Hence, the attenuation function \$f(\alpha)\$ is added into (15) to revise the pressure-related force

$$F_p = f(\alpha) \frac{\sqrt{3}(2a^2 + 5ab + 2b^2)}{6} P \quad (16)$$

where \$f(\alpha)\$ is calibrated experimentally. Overall, the axial generated force \$F_a\$ of the actuator is

$$F_a = f(\alpha) \frac{\sqrt{3}(2a^2 + 5ab + 2b^2)}{6} P - k\Delta l_i. \quad (17)$$

2) Modeling for Bending Torque \$T_a\$: The exerted torque on the actuator results in the new balanced configuration for the actuator, as shown in Fig. 4(a). According to assumption 6), the works done by pressure and external force are zero, so \$\delta W_S = \delta W_{T_e}\$. The generated bending torque \$T_a\$ equals \$T_e\$, which means the bending torque only depends on the actuator's self-deformation, where the length of the left layer increases while the length of the right layer decreases, as shown in Fig. 4(a). Hence, bending torque can be derived as

$$\begin{aligned} T_a &= \sum_{m=1} F_{cm} \frac{d_a}{2} \cos \vartheta \\ &= \int_C \frac{k \cdot ds}{\pi d_a} (l_0 - l_c) \frac{d_a}{2} \cos \vartheta = \frac{kd_a^2 \alpha}{8} \end{aligned} \quad (18)$$

where \$l_c\$ is the length of the actuator's edge, path \$C\$ is the actuator's equivalent circular edge, and \$l_c = l_i - \alpha d_a / 2 \cos \vartheta\$ based on the geometric relation in Fig. 4(a).

D. Joint Force Modeling

The joint-level force model JFM will be carried out in this section based on the soft AFM, as shown in Fig. 3(a). We apply \$F_i\$ and \$T_i\$ to denote the generated force and torque of the \$i\$th actuator in the soft joint and use \$\mathbf{F}_i\$ and \$\mathbf{T}_i\$ to represent the force and torque vector. When the soft robot is in a balanced state, the accumulated external force and generated force will be equal, and then, total external general forces can be obtained. As shown in Fig. 3(d), the actuators' bending angles \$\alpha\$ are the same and equal to the joint's bending angle \$\beta = \kappa L\$. Therefore

$$\begin{aligned} F_i &= f(\beta) \frac{\sqrt{3}(2a^2 + 5ab + 2b^2)}{6} P_i - k_i \Delta l_i \\ T_i &= \frac{k_i d_a^2 \beta}{8} \end{aligned} \quad (19)$$

where \$P_i\$, \$k_i\$, and \$\Delta l_i\$ are the installed \$i\$th actuator's pressure, stiffness, and relative length, respectively. Based on force and torque translation along the installed rigid plane, we also derive

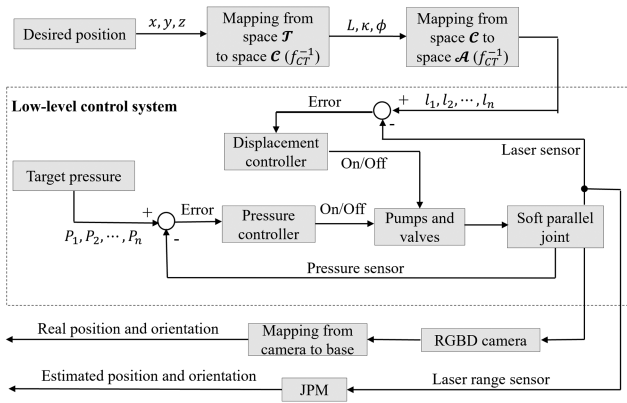


Fig. 5. Control strategy for the parallel soft joint.

\mathbf{F} and torque vector \mathbf{T} as

$$\mathbf{F} = \sum_{i=1}^n \mathbf{F}_i, \quad \mathbf{T} = \sum_{i=1}^n (\mathbf{r}_i \times \mathbf{F}_i) + \sum_{i=1}^n \mathbf{T}_i \quad (20)$$

where \mathbf{r}_i is actuator's mounting position from O_1 for the i th actuator. For the OSPJ, by substituting (19) into (20), the external force, axial direction F_z , and radial torque T_x, T_y , as shown in Fig. 3(d), can be realized as follows:

$$\begin{aligned} F_z &= \sum_{i=1}^4 F_i, \quad T_x = \sum_{i=1}^4 T_i \sin \phi + \frac{d_s}{2} (F_2 - F_4) \\ T_y &= - \sum_{i=1}^4 T_i \cos \phi - \frac{d_s}{2} (F_1 - F_3). \end{aligned} \quad (21)$$

V. SYSTEM AND CONTROL SCHEME

To demonstrate the above methods, we design a control system for the OSPJ, as shown in Fig. 5. The displacement controller makes the soft joint realize accurate position control even with external stimuli, while the pressure controller can keep the soft joint compliant, especially for interaction tasks. Once the target positions of the joint or target pressures for each actuator are provided, the joint can reach the desired targets by adjusting the actuator's internal pressure. The soft joint's real-time states can be measured by the installed external RGBD camera directly and perceived by the built-in sensors through the JPM model indirectly. The low-level control system runs in the microcontroller, and the trajectory planning algorithm is realized by MATLAB and Qt software on the PC. More details on the low-level control system can be found in our previous works as well [5], [25].

To implement the control scheme, each actuator's target displacement should be computed first from the desired position of the joint. Hence, based on (7), we can obtain the related configuration variables in space \mathcal{C}

$$\phi = \arctan \left(\frac{y}{x} \right), \quad \kappa = \frac{2x \cos \phi}{x^2 + z^2 \cos^2 \phi}, \quad L = \frac{\arcsin \kappa z}{\kappa}. \quad (22)$$

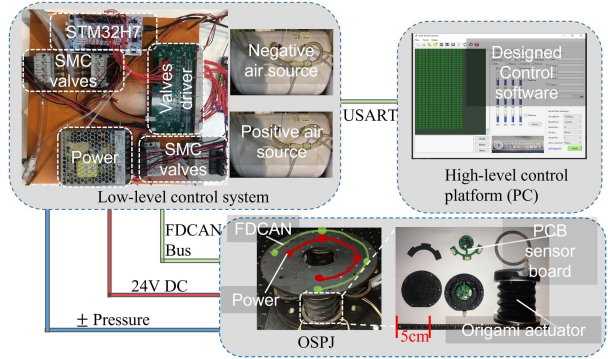


Fig. 6. Control system for the OSPJ.

Second, f_{AC}^{-1} , mapping configuration variables to actuator variables, can be computed by substituting (22) into (1). Specifically, when $n = 4$

$$l_i = L \left(1 + (-1)^i \frac{\kappa d_s}{2} \sin \left(\phi + \frac{i\pi}{2} \right) \right) \quad (23)$$

where ϕ , κ , and L are derived in (22), and $i = 1, 2, 3, 4$. As shown in Fig. 1(c), the laser range sensor measures the distance l_{mi} in Fig. 3(c). We revise the real length with $L = \frac{\tan(L\kappa)}{\kappa}$ in (23).

VI. EXPERIMENTS AND RESULTS

We first present the control system for the soft joint. Then, the self-sensing origami actuator's characteristic experiment is conducted, followed by the bending experiment to validate the AFM. Finally, the JPM and JFM are demonstrated by several path-tracking and force interaction experiments.

A. Joint Control System

As shown in Fig. 6, the system consists of three parts: OSPJ, low-level control system, and high-level control system on PC. The soft joint contains four soft origami actuators with a dedicated sensor board, consisting of an air pressure sensor (FXPS7550DI4T1, NXP Semiconductors, Eindhoven, The Netherlands) and a laser range sensor (VL6180XV0NR1, STMicroelectronics, Geneva, Switzerland). The soft joint's bending angle is restricted within 30°, to guarantee that the laser range sensor reaches the actuator's end. All sensors are encoded into a data package, being broadcasted to the low-level microcontroller (NUCLEO-H743Z12, STMicroelectronics, Geneva, Switzerland) through FDCAN protocol, with a baud rate of 1 Mb/s. The low-level controller operates the solenoid valves (VQD1151W-5L, SMC, Indianapolis, IN, USA) to adjust each actuator's air pressure. Considering large internal pressure leads to the actuator's inevitable radial deformation, we set a working pressure range as (-60 kPa, 60 kPa), ensuring the origami actuator's linear characteristic [23], [34]. The system has eight individual control channels driven by the designed valve driver. Also, it receives the objective pressure or displacement generated by a high-level PC and transfers each actuator's state to the PC. The high-level control software is also developed to control

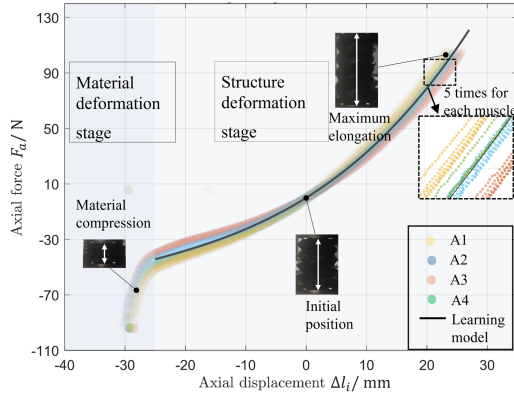


Fig. 7. Axial force F_a versus the actuators' self-deformation Δl_i . Five repeat experiments for each actuator.

the soft actuator and soft robot. The control frequency and sampling frequency are all set at 100 Hz, and the communication delay between the microcontroller and the sensor board is around 2 ms. The displacement and pressure deadzone for the low-level control are 1.2 mm and 1.0 kPa, respectively. Due to the voltage drop, the maximum number of the PDDSA is 36.

B. Performance of the PDDSA

As with the experimental setup designed in [25] to study the actuator's characteristics, the same one is also introduced. Four actuators are selected randomly to reduce the effect of manufacturing error. The main geometry parameters of the selected actuator are illustrated in Table I. More manufacturing processes can refer to our previous works [5], [25]. In this work, we redesign its sealing to improve the actuator's reliability and the embedded sensor board's reusability, as shown in Fig. 6. As shown in Fig. 7, the actuator's deformation is divided into two stages: the material deformation and the desired structure deformation. The actuator's working range is almost ± 25 mm from the initial position. The actuator's stiffness k is nonlinear with respect to Δl_i , and it is fitted by a simple polynomial within the working range as follows:

$$F_a = -k\Delta l_i = -(c_2\Delta l_i^2 + c_1\Delta l_i + c_0)\Delta l_i. \quad (24)$$

The average coefficients in (24) are $c_2 = 0.0005$, $c_1 = 0.0511$, and $c_0 = 2.7148$, with stiffness deviation of 0.345 N/mm.

The experimental setup for the actuator's bending torque and force over different input pressure at the specific bending angle is shown in Fig. 8. Two mechanical plates are fixed to achieve the desired bending angle: one is manufactured by 3-D printed PLA, and the other is made of metal. A force sensor (Nano17 IP68, ATI Industrial Automation, Apex, NC, USA) is mounted at the actuator's active end to measure output force and torque. An IMU (BNO055, Bosch Tools, Mount Prospect, IL, USA) is also added to the sensor board to measure the actuator's bending angle. The assembly and self-sensing performance of the PDDSA are shown in Video S1, available in the online supplementary material.

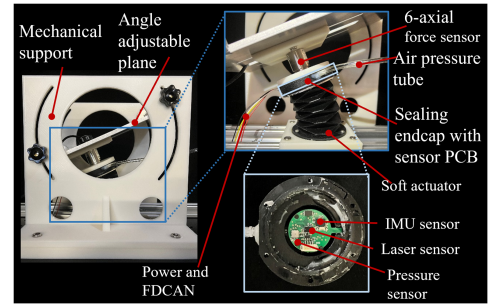


Fig. 8. Bending experimental setup.

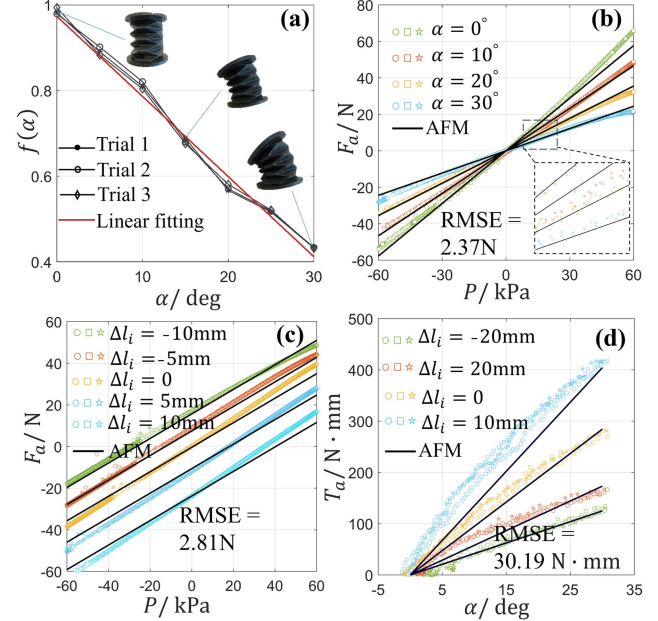


Fig. 9. (a) Attenuation function $f(\alpha)$ is calibrated from the origami actuator at six bending states. (b) Generated force over input pressure at initial length with different α . (c) Force over input pressure with various length l_i at $\alpha = 20^\circ$. (d) Torque over bending angle α with various length l_i .

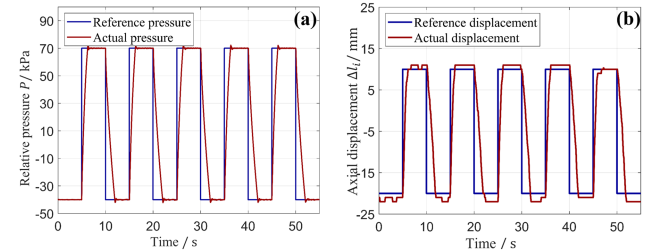


Fig. 10. (a) Pressure and (b) displacement control performance.

We first study the axial force F_a over input relative pressure P at six selected bending situations with the range of $(0, 30^\circ)$, to calibrate the attenuation function $f(\alpha)$ in (17). We use the linear model to fit the experimental results, as shown in Fig. 9(a). The attenuation function is calibrated as $f(\alpha) = -0.0188\alpha + 0.971$. Then, three bending experiments for the actuator are conducted to validate our proposed AFM in (17) and (18). As shown in Fig. 9(b), we set the actuator's length

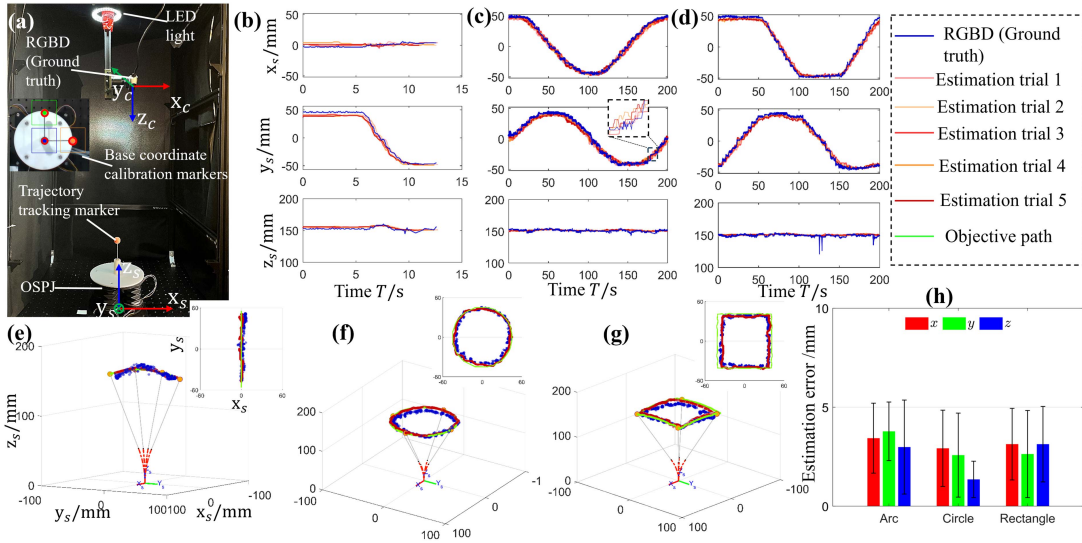


Fig. 11. (a) Joint position perception experimental setup. (b)–(d) Real-time position for arc, circle, and rectangle trajectory. (e)–(g) Arc, circle, and rectangle trajectory tracking. (h) Position estimation error for path-tracking experiments.

l_i as l_0 and study F_a over P at four given different α , with the minimum root-mean-square error (RMSE) of 2.371 N between the AFM and the experimental results. Then, the bending angle stays at $\alpha = 20^\circ$ and conducts axial force F_a over P at five given different Δl_i , with the RMSE of 2.808 N. Finally, the generated torque T_a related to actuator's bending angle α at different lengths Δl_i is plotted in Fig. 9(d). Although the relationship is not strictly linear in the experiment, the linear model can obtain promising results within $\alpha \leq 30^\circ$ with the RMSE of 30.19 N · mm.

To verify the presented low-level control scheme for the PDDSA with the built-in sensors in Section IV, the pressure and displacement control experiments are conducted. Fig. 10(a) shows a square pressure reference wave with pressures of -40 and 70 kPa, respectively. Fig. 10(b) shows a square displacement reference wave with displacements of -20 and 10 mm, respectively. Video S2 shows the pressure and displacement control performances.

C. Spatial Position and Force Perception Performance

1) *Spatial Position Perception:* The experimental setup for position estimation is shown in Fig. 11(a). We utilize an RGBD camera (Depth Camera D435i, Intel RealSense, Santa Clara, CA, USA) to provide the ground truth, with depth RMSE being calibrated around 1 mm. The blue, orange, and green markers with a diameter of 20 mm are installed to compute the transformation matrix from the camera to the base coordinate system. The markers are detected by combining HoughCircles and findContours functions in OpenCV-4.5.3. Then, the only orange ball is tracked. The whole process is achieved via the control strategy, as shown in Fig. 5. The camera's sampling frequency and communication frequency in USART are set as 30 Hz. The objective points are sent from the PC at 2 Hz. We set

TABLE II
POSITION AND AXIAL FORCE ESTIMATION ERROR (RMSE) OF SPATIAL POINT WITHIN WORKSPACE

β ($^\circ$)	0	5	10	15	20	25	30
Position (mm)	2.1 ± 1.3	2.2 ± 1.2	2.4 ± 1.2	2.5 ± 1.3	2.7 ± 1.4	2.8 ± 1.3	2.8 ± 1.4
Axial force (N)	2.51 ± 1.05	2.53 ± 1.11	2.60 ± 1.23	2.81 ± 1.31	3.19 ± 1.23	3.15 ± 1.24	3.56 ± 1.34
L (mm)	25	35	45	50	55	65	75
Position (mm)	2.4 ± 1.4	2.2 ± 1.3	2.3 ± 1.3	2.1 ± 1.2	2.1 ± 1.1	2.0 ± 1.3	2.1 ± 1.4
Axial force (N)	3.86 ± 1.45	3.56 ± 1.32	2.48 ± 1.43	2.51 ± 1.05	2.89 ± 1.62	3.56 ± 1.38	3.97 ± 1.41

three trajectories, arc, circle, and rectangle in the experiments, and each experiment is tested five times.

As shown in Fig. 11(e)–(g), the red dashed line is the soft joint's backbone. The x, y, z coordinates of the orange ball in frame $\{s\}$ over time are also presented in Fig. 11(b)–(d). Detailed displacements over time for actuators can be found in Video S3. The absolute error between the estimation and ground truth is plotted in Fig. 11(h). The mean of the position error is 2.8 mm with a standard deviation of 1.1 mm. More details about the position perception performance are attached in Video S3.

2) *Spatial Force Perception:* To validate the JFM F_z, T_x, T_y in (21), we conduct force perception experiments for the soft joint, where the interactive forces are measured by the commercial force sensor (Nano17 IP68, ATI Industrial Automation, Apex, NC, USA) as the ground truth, as shown in Fig. 12. The z -axis force of the force sensor is only utilized due to its limited measurable torque range (0–500 N · mm). The exerted force F_e is measured by the force sensor directly to validate F_z , as shown in Fig. 12(a). As shown in Fig. 12(b) and (c), the exerted torques T_{ex} and T_{ey} are computed by $F_e L_e$ indirectly to validate T_x and T_y , where L_e is the installation distance of the force sensor, $L_e = 60$ mm. As shown in Fig. 13, the force estimation scheme

TABLE III
COMPARISONS TO THE STATE-OF-THE-ART POSITION AND FORCE PERCEPTION WITH EMBEDDED SENSORS

Robotic platform	DoFs	Material	Actuation	Deformation	Sensors	Approach	Platform	Experimental description (states)	Position NRMSE	Force NRMSE	Torque NRMSE
Soft finger [1]	1	Soft elastomer	Pneumatic	Bending	Soft strain sensors, pressure sensors	LSTM	Desktop computer	Tip and middle position, horizontal force	9.5%	15.3%	-
Soft gripper [2]	1	Polyethylene	Pneumatic	Elongation, shorten	Pressure sensors	Analytical models	Single-board or desktop computer	Open distance, grasping force	2.6%	7.8%	-
Soft finger [18]	1	Silicone rubber	Pneumatic	Bending	Embedded flex sensors, pressure sensors	RNN-AUKF	Desktop computer	Segmental bending angles, horizontal and vertical forces	4.6%	12.0%	-
OSPJ (Our work)	3	Polypropylene rubber	Pneumatic	Bending, elongation, shorten	Embedded pressure and laser sensors	Analytical models	Single-board or desktop computer	3D position, force along the backbone, bending torques	3.3%	7.2%	7.1%

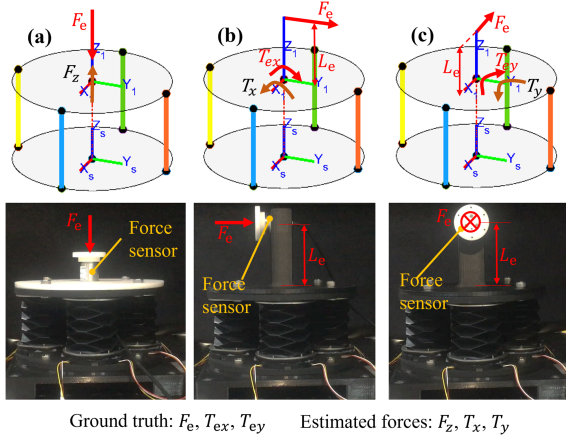


Fig. 12. (a)–(c) Joint force estimation experimental setup for F_z , T_x , and T_y in (21).

is validated in three cases with representative initial states. We first adjust the joint to the three desired positions and close all valves to maintain the states. Then, the external stimuli are exerted on the joint.

The repeat experiments for case 1 are first conducted to validate the repeatability, as shown in Fig. 13(a). The results are shown in Fig. 13(b)–(d). Detailed pressures and displacements for actuators are attached to Video S4. The estimated forces and torques are close to zero at $T = 0$ s. The predicted force deviations from the actuator's stiffness deviations (actuator manufacture difference) are 1.32 N, 55.14 N · mm, and 59.37 N · mm for F_z , T_x , and T_y , respectively. As shown in Fig. 13(e), the mean of the force error is 3.4 N with a standard deviation of 2.7 N, and the mean of the torque error is 196.3 N · mm with a standard deviation of 174.89 N · mm.

In the soft robots with the PDDSA, the force observer shows a lag behind the ground truth. This lag behavior is mainly due to the slower dynamic of the soft sensors and can be calibrated experimentally [1]. The phase lag's effect is presented in Fig. 14. The fixed-input lag for the soft joint is hand-tuned as 450 ms experimentally. The lag-free force error and torque is 2.7 N with a standard deviation of 0.68 N, and the lag-free torque error is 137.5 N · mm with a standard deviation of 51.23 N · mm. In addition, spatial position and force experiments for a single point within the workspace are carried out to demonstrate the effectiveness of the proposed method, as shown in

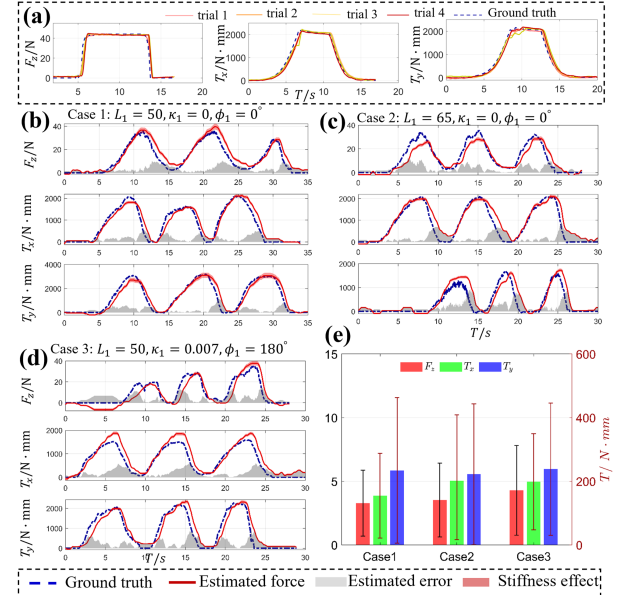


Fig. 13. (a) Four repeat force perception experiments for F_z , T_x , and T_y . (b)–(d) Soft joint spatial force perception experimental results for case 1, case 2, and case 3. (e) Force perception error.

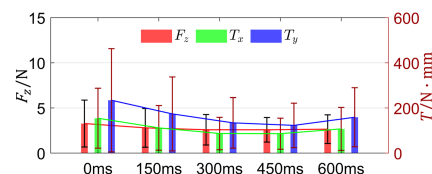


Fig. 14. Phase lag's effect on force error for Case 1.

Table II. Under random lateral disturbances to the soft actuator, the soft robot's position and force estimation RMSE are 2.5 mm and 10.6 N, respectively. The force prediction is more easily affected by the actuator's lateral disturbance as the actuator's deformation changes the internal air pressure.

We compare our work to the state-of-the-art soft robots' position–force perception solutions in terms of DoFs, material, deformation, sensors, estimation approach, and so on in Table III. The normalized RMSE (NRMSE) [18], calculated as the RMSE divided by the range of the observed values, is also computed for the estimated positions and forces.

The NRMSEs of the position, force, and torque in our proposed method are 3.3%, 7.2%, and 7.1%, respectively. The high-dimensional perception scheme can achieve a promising performance for the three-DoF soft robot, providing the potential for soft robots to realize position and force feedback control.

VII. CONCLUSION

This article presents a novel scheme for achieving the spatial simultaneous position and force perception for soft parallel robots based on the PDDSA. Inspired by the human muscle receptors, a built-in sensing module with pressure and laser sensor chips is designed to measure the real-time states. The three-DoF soft parallel robot with the maximum bending angle of 30° is developed based on the PDDSA to implement the spatial perception. To this end, the actuator-level force models and the joint-level position and force models are derived analytically to endow the soft robot with the 3-D position and three-axial force estimations. Compared to the state-of-the-art works, the estimated position and force can present promising performances, with the position, force, and torque NRMSEs of 3.3%, 7.20%, and 7.07%, respectively.

The sensing module demonstrated in this article exhibits no complicated fabrication or compromise in compliance and is easily embedded into the soft elastic actuator. The actuator is easy to replace when it suffers from leaks, breakage, and fatigue without remanufacturing. Although the soft parallel joint is proposed to demonstrate the high-dimensional perceptive strategy, the soft joint with the actuator- and joint-level perception methods based on the PDDSA can be easily assembled as a soft robotic manipulator. Moreover, the PDDSA can be convenient to assemble in various configurations, providing a cost-effective path for realizing intelligent control without other expensive sensors.

One limitation of this work is that dynamic effects on the perceptions are not considered, as the quasi-static assumption is made for the force models. The other limitation is that the hand-tuned phase lag should be preset (450 ms in the OSPJ) to improve the performance. It depends on the material characteristics of the soft actuator and should be calibrated experimentally. Moreover, the proposed perceptive method is validated in the soft parallel robot with the preset workspace (axial motion: ± 25 mm, bending angle: $\leq 30^\circ$); more applications should be extended to soft robots with larger workspaces.

Future works should also investigate graceful degradation and related control algorithms. In addition, a multisegment soft manipulator based on the perceivable soft joint should be developed to demonstrate the applicability of the method.

REFERENCES

- [1] T. G. Thuruthel, B. Shih, C. Laschi, and M. T. Tolley, "Soft robot perception using embedded soft sensors and recurrent neural networks," *Sci. Robot.*, vol. 4, no. 26, 2019, Art. no. eaav1488.
- [2] L. Wang and Z. Wang, "Mechanoreception for soft robots via intuitive body cues," *Soft Robot.*, vol. 7, no. 2, pp. 198–217, 2020.
- [3] Y. Su, Y. Wang, and A. Kheddar, "Sample-efficient learning of soft task priorities through Bayesian optimization," in *Proc. IEEE Int. Conf. Humanoid Robots*, 2018, pp. 1–6.
- [4] Z. Wang, S. Liu, J. Peng, and M. Z. Chen, "The next-generation surgical robots," in *Surgical Robotics*. London, U.K.: IntechOpen, 2018, p. 1.
- [5] J. Li, X. Chen, Y. Su, W. Wang, J. Lam, and Z. Wang, "Kinematic analysis of soft continuum manipulators based on sparse workspace mapping," *IEEE Robot. Autom. Lett.*, vol. 7, no. 2, pp. 5055–5062, Apr. 2022.
- [6] W. Zhu et al., "A soft-rigid hybrid gripper with lateral compliance and dexterous in-hand manipulation," *IEEE/ASME Trans. Mechatron.*, vol. 28, no. 1, pp. 104–115, Feb. 2023.
- [7] J. Lai, B. Lu, and H. K. Chu, "Variable-stiffness control of a dual-segment soft robot using depth vision," *IEEE/ASME Trans. Mechatron.*, vol. 27, no. 2, pp. 1034–1045, Apr. 2022.
- [8] H. Jiang et al., "Hierarchical control of soft manipulators towards unstructured interactions," *Int. J. Robot. Res.*, vol. 40, no. 1, pp. 411–434, 2021.
- [9] R. Yasin and N. Simaan, "Joint-level force sensing for indirect hybrid force/position control of continuum robots with friction," *Int. J. Robot. Res.*, vol. 40, nos. 4/5, pp. 764–781, 2021.
- [10] R. Hashem, M. Stommel, L. K. Cheng, and W. Xu, "Design and characterization of a bellows-driven soft pneumatic actuator," *IEEE/ASME Trans. Mechatron.*, vol. 26, no. 5, pp. 2327–2338, Oct. 2021.
- [11] M. Luo et al., "Toward modular soft robotics: Proprioceptive curvature sensing and sliding-mode control of soft bidirectional bending modules," *Soft Robot.*, vol. 4, no. 2, pp. 117–125, 2017.
- [12] Z. Wang, P. Polygerinos, J. T. Overvelde, K. C. Galloway, K. Bertoldi, and C. J. Walsh, "Interaction forces of soft fiber reinforced bending actuators," *IEEE/ASME Trans. Mechatron.*, vol. 22, no. 2, pp. 717–727, Apr. 2017.
- [13] C. Tawk, E. Sarıyıldız, and G. Alici, "Force control of a 3D printed soft gripper with built-in pneumatic touch sensing chambers," *Soft Robot.*, vol. 9, no. 5, pp. 970–980, 2022.
- [14] G. Alici, T. Canty, R. Mutlu, W. Hu, and V. Sencadas, "Modeling and experimental evaluation of bending behavior of soft pneumatic actuators made of discrete actuation chambers," *Soft Robot.*, vol. 5, no. 1, pp. 24–35, 2018.
- [15] R. B. Scharff, R. M. Doornbusch, E. L. Doubrovski, J. Wu, J. M. Geraedts, and C. C. Wang, "Color-based proprioception of soft actuators interacting with objects," *IEEE/ASME Trans. Mechatron.*, vol. 24, no. 5, pp. 1964–1973, Oct. 2019.
- [16] R. B. Scharff, G. Fang, Y. Tian, J. Wu, J. M. Geraedts, and C. C. Wang, "Sensing and reconstruction of 3-D deformation on pneumatic soft robots," *IEEE/ASME Trans. Mechatron.*, vol. 26, no. 4, pp. 1877–1885, Aug. 2021.
- [17] Z. Fang et al., "Multi-dimensional proprioception and stiffness tuning for soft robotic joints," in *Proc. IEEE Int. Conf. Robot. Autom.*, 2022, pp. 10973–10979.
- [18] J. Y. Loo, Z. Y. Ding, V. M. Baskaran, S. G. Nurzaman, and C. P. Tan, "Robust multimodal indirect sensing for soft robots via neural network-aided filter-based estimation," *Soft Robot.*, vol. 9, no. 3, pp. 591–612, 2022.
- [19] L. Wang et al., "Soft robot proprioception using unified soft body encoding and recurrent neural network," *Soft Robot.*, vol. 10, no. 4, pp. 825–837, 2023.
- [20] H. Zhao, K. O'brien, S. Li, and R. F. Shepherd, "Optoelectronically innervated soft prosthetic hand via stretchable optical waveguides," *Sci. Robot.*, vol. 1, no. 1, 2016, Art. no. eaai7529.
- [21] R. L. Truby et al., "Soft somatosensitive actuators via embedded 3D printing," *Adv. Mater.*, vol. 30, no. 15, 2018, Art. no. 1706383.
- [22] V. Falkenhahn, A. Hildebrandt, R. Neumann, and O. Sawodny, "Dynamic control of the bionic handling assistant," *IEEE/ASME Trans. Mechatron.*, vol. 22, no. 1, pp. 6–17, Feb. 2017.
- [23] C. Tawk, H. Zhou, E. Sarıyıldız, M. I. H. Panhuis, G. M. Spinks, and G. Alici, "Design, modeling, and control of a 3D printed monolithic soft robotic finger with embedded pneumatic sensing chambers," *IEEE/ASME Trans. Mechatron.*, vol. 26, no. 2, pp. 876–887, Apr. 2021.
- [24] H. Yang, Y. Chen, Y. Sun, and L. Hao, "A novel pneumatic soft sensor for measuring contact force and curvature of a soft gripper," *Sens. Actuator A: Phys.*, vol. 266, pp. 318–327, 2017.
- [25] Y. Su et al., "A high-payload proprioceptive hybrid robotic gripper with soft origamic actuators," *IEEE Robot. Autom. Lett.*, vol. 5, no. 2, pp. 3003–3010, Apr. 2020.
- [26] G. Fang, Y. Tian, Z.-X. Yang, J. M. Geraedts, and C. C. Wang, "Efficient Jacobian-based inverse kinematics with sim-to-real transfer of soft robots by learning," *IEEE/ASME Trans. Mechatron.*, vol. 27, no. 6, pp. 5296–5306, Dec. 2022.
- [27] D. Bruder, X. Fu, R. B. Gillespie, C. D. Remy, and R. Vasudevan, "Data-driven control of soft robots using Koopman operator theory," *IEEE Trans. Robot.*, vol. 37, no. 3, pp. 948–961, Jun. 2021.

- [28] M. O. Williams, I. G. Kevrekidis, and C. W. Rowley, "A data-driven approximation of the Koopman operator: Extending dynamic mode decomposition," *J. Nonlinear Sci.*, vol. 25, pp. 1307–1346, 2015.
- [29] W. Ouyang, L. He, A. Albini, and P. Maiolino, "A modular soft robotic arm with embedded tactile sensors for proprioception," in *Proc. IEEE Int. Conf. Soft Robot.*, 2022, pp. 919–924.
- [30] Z. Gong et al., "A soft manipulator for efficient delicate grasping in shallow water: Modeling, control, and real-world experiments," *Int. J. Robot. Res.*, vol. 40, no. 1, pp. 449–469, 2021.
- [31] X. Huang, J. Zou, and G. Gu, "Kinematic modeling and control of variable curvature soft continuum robots," *IEEE/ASME Trans. Mechatron.*, vol. 26, no. 6, pp. 3175–3185, Dec. 2021.
- [32] C. Tutcu, B. A. Baydere, S. K. Talas, and E. Samur, "Quasi-static modeling of a novel growing soft-continuum robot," *Int. J. Robot. Res.*, vol. 40, no. 1, pp. 86–98, 2021.
- [33] U. Proske and S. C. Gandevia, "The proprioceptive senses: Their roles in signaling body shape, body position and movement, and muscle force," *Physiol. Rev.*, vol. 92, pp. 1651–1697, 2012.
- [34] L. Paez, G. Agarwal, and J. Paik, "Design and analysis of a soft pneumatic actuator with origami shell reinforcement," *Soft Robot.*, vol. 3, no. 3, pp. 109–119, 2016.
- [35] A. Zaghloul and G. M. Bone, "3D shrinking for rapid fabrication of origami-inspired semi-soft pneumatic actuators," *IEEE Access*, vol. 8, pp. 191330–191340, 2020.



Yinyin Su received the B.Eng. degree in engineering mechanics from Northeastern University, Shenyang, China, in 2014, and the M.Sc. degree in general and fundamental mechanics from the Institute of Mechanics, Chinese Academy of Sciences, Beijing, China, in 2017. He is currently working toward the Ph.D. degree with the Department of Mechanical Engineering, The University of Hong Kong, Hong Kong.

He is also with the Department of Mechanical and Energy Engineering, Southern University of Science and Technology, Shenzhen, China. His research interests include soft robotics, modeling and perception for soft robots, control and optimization, and artificial intelligence.



Dong Liu received the B.S. degree in electronic and information engineering from South-Central Minzu University For Nationalities, Wuhan, China, in 2014.

He is currently a Research Engineer with the Department of Mechanical Engineering and Energy Engineering, Southern University of Science and Technology, Shenzhen, China.



James Lam (Fellow, IEEE) received the B.Sc. (Hons.) degree in mechanical engineering from the University of Manchester, Manchester, U.K., in 1983, and the M.Phil. degree in control engineering and operational research and the Ph.D. degree in control engineering from the University of Cambridge, Cambridge, U.K., in 1985 and 1988, respectively.

He was a Faculty Member at the City University of Hong Kong, Hong Kong, and the University of Melbourne, Parkville, VIC, Australia.

In 1993, he joined the University of Hong Kong, where he is currently a Chair Professor in control engineering. He is currently a Croucher Scholar, Croucher Fellow, and Distinguished Visiting Fellow of the Royal Academy of Engineering and Cheung Kong Chair Professor. His research interests include multiagent systems, positive systems, Boolean networks, networked control systems, and vibration control.

Dr. Lam is a Chartered Mathematician (CMath), Chartered Scientist (CSci), Chartered Engineer (CEng), Fellow of Institute of Electrical and Electronic Engineers (FIEEE), Fellow of Institution of Engineering and Technology (FIET), Fellow of Institute of Mathematics and Its Applications (FIMA), Fellow of Institution of Mechanical Engineers (FIMechE), Fellow of Hong Kong Institution of Engineers (FHKIE), and Fellow of Asia-Pacific Artificial Intelligence Association (FAAIA). He was the recipient of the Ashbury Scholarship, A.H. Gibson Prize, and H. Wright Baker Prize for his academic performance. He is a Highly Cited Researcher in engineering (2014 to 2020), computer science (2015), and cross-fields (2021).



Xiaojiao Chen received the B.Eng. degree in mechanical engineering from the Huazhong University of Science and Technology, Wuhan, China, in 2012, and the M.S. degree in mechanical engineering in 2015 from The University of Hong Kong, Hong Kong, where he is currently working toward the Ph.D. degree in soft robotics.

His research interests include soft actuators, soft robotic arms, variable stiffness control, and human–robot interaction.



Zheng Wang (Senior Member, IEEE) received the B.Sc. (Hons.) degree in automatic control from Tsinghua University, Beijing, China, in 2004, the M.Sc. (Hons.) degree in control systems from Imperial College London, London U.K., in 2005, and the Ph.D. (Hons.) degree in electrical engineering from Technische Universitaet Muenchen, Munich, Germany, in 2010.

From 2010 to 2013, he was a Postdoctoral Research Fellow with Nanyang Technological University, Singapore. He was a Postdoctoral Fellow with the School of Engineering and Applied Sciences and the Wyss Institute of Bioinspired Engineering, Harvard University, Cambridge, MA, USA, in 2013 and 2014, respectively. Since 2014, he has been an Assistant Professor with the Department of Mechanical Engineering, The University of Hong Kong, Hong Kong. Since 2019, he has been a Professor of Robotics with the Department of Mechanical and Energy Engineering, Southern University of Science and Technology, Shenzhen, China. His research interests include haptics human–robot interaction, endoscopic surgical robot, underwater robots, and soft robotics.



Zhonggui Fang received the B.S. degree in mechanical design manufacturing and automation from the Guangdong University of Technology, Guangzhou, China, in 2019. He is currently working toward the Ph.D. degree in intelligent manufacturing and robotics with the Department of Mechanical Engineering and Energy Engineering, Southern University of Science and Technology, Shenzhen, China.

His research interests include soft robotics and biomimetic robot.